



Final Draft **of the original manuscript**

Li, Y.; Zhao, D.; Liu, J.; Qian, S.; Li, Y.; Gan, W.; Chen, X.:

Energy-Efficient Elastocaloric Cooling by Flexibly and Reversibly Transferring Interface in Magnetic Shape-Memory Alloys.

In: ACS Applied Materials and Interfaces. Vol. 10 (2018) 30, 25438 - 25445.

First published online by ACS: 10.07.2018

<https://dx.doi.org/10.1021/acsami.8b07703>

Energy-efficient Elastocaloric Cooling by Flexibly and Reversibly Transferring Interface in Magnetic Shape Memory Alloys

Yang Li^{†¶}, Dewei Zhao^{†‡¶}, Jian Liu^{†‡*}, Suxin Qian^{§*}, Zongbin Li^{//}, Weimin Gan⁺, and Xian Chen[#]

[†]CAS Key Laboratory of Magnetic Materials and Devices, and Zhejiang Province Key Laboratory of Magnetic Materials and Application Technology, Ningbo Institute of Materials Technology and Engineering, Chinese Academy of Sciences, Ningbo 315201, China

[‡]University of Chinese Academy of Sciences, 19 A Yuquan Rd, Shijingshan District, Beijing 100049, China

[§]Department of Refrigeration and Cryogenic Engineering, School of Energy and Power Engineering, Xi'an Jiaotong University, Xi'an 710049, China

^{//}Key Laboratory for Anisotropy and Texture of Materials (Ministry of Education), Northeastern University, Shenyang 110819, China

⁺German Engineering Materials Science Centre (GEMS), Helmholtz-Zentrum Geesthacht (HZG) Outstation at FRM II, D-85748 Garching, Germany

[#] Department of Mechanical and Aerospace Engineering, Hong Kong University of Science and Technology, Clear Water Bay, Hong Kong

ABSTRACT: Elastocaloric cooling is currently under extensive study owing to its great potential to replace the conventional vapor-compression technique. In this work, by employing multiscale characterization approaches, including in situ neutron diffraction in a loading frame, in situ transmission electron microscope observation at different temperatures, in situ synchrotron X-ray Laue micro-diffraction, and high-resolution infrared thermo-imaging, we have investigated the thermal and stress induced martensitic transformation, the stability of superelastic behavior and associated elastocaloric effect for a Heusler-type $\text{Ni}_{50.0}\text{Fe}_{19.0}\text{Ga}_{27.1}\text{Co}_{3.9}$ single crystal. Based on the transformation from cubic austenite to monoclinic martensite with a flexibly and reversibly transferring interface, this unique single crystal exhibits giant elastocaloric effect of 11 K and ultralow fatigue behavior during above 12,000 mechanical cycles. The numerical simulation shows that the $\text{Ni}_{50.0}\text{Fe}_{19.0}\text{Ga}_{27.1}\text{Co}_{3.9}$ alloy offers 18% energy saving potential and 70% cooling capacity enhancement potential than the conventional shape memory nitinol alloy in a single-stage elastocaloric cooling system, making it as a great candidate for the energy-efficient air conditioner application.

KEYWORDS: *superelasticity, elastocaloric effect, Ni-Fe-Ga-Co, martensitic transformation, magnetic shape memory alloys*

■ INTRODUCTION

Refrigeration and air conditioning represent nearly 20% energy consumption of the electricity demands in the world.¹ While the vapor-compression technology has effectively served the cooling needs for close to 100 years, the refrigerants used in the vapor-compression system have detrimental effects on the global climate change when released to the atmosphere. Although some new refrigerants with almost negligible greenhouse effect (e.g. R1234yf) have been explored, these refrigerants are flammable in large quantities. Therefore, there is still an urgent need for subversive cooling technique to replace conventional ones. In the past decade, there has been a surge in the research of reversible thermal changes of eco-friendly caloric materials in response to different external stimuli.²⁻⁸ By applying electric field, magnetic field and uniaxial stress, these thermal changes are accordingly named as electrocaloric, magnetocaloric and elastocaloric effects.³⁻⁴ In terms of room temperature solid-state refrigerator, the magnetocaloric and electrocaloric refrigeration prototypes are relatively widely designed compared to elastocaloric one.⁹⁻¹¹ However, the high cost of magnets for magnetocaloric technique is still a bottleneck issue for its commercialization. Considering the relatively low adiabatic temperature change and energy conversion efficiency for electrocalorics, it exhibits limited potential in the application of high cooling capacity air conditioners. Due to its large energy saving potential and high energy efficiency, the emerging elastocaloric effect opens up a new route for room temperature refrigeration.¹²⁻¹³ For a heat pump, refrigerator or air conditioner, the ratio of useful heating or cooling provided to work required is referred to as the coefficient of performance (COP). A high COP means a low operating cost. Compared with a COP of around 3.2 for the baseline of vapor-compression systems, a COP of 3.7-4.9 for electrocaloric refrigeration and a potential COP of 2-4 for magnetocaloric cooling system, elastocaloric refrigeration has a high potential COP up to approximately 12.¹³ This makes elastocaloric effect as a promising alternative refrigeration technology that attracts growing attention.

In recent years, the large elastocaloric effect during martensitic transformation has been reported in plenty of shape memory alloys (SMAs), such as Ni-Ti,^{8,12,14} Cu-Zn-Al,¹⁵ Ni-Fe-Ga,¹⁶⁻¹⁸ Fe-Pd,¹⁹ and Ni-Mn-based alloys.²⁰⁻²¹ However, the key challenges for current caloric materials in practical cooling application are energy conversion efficiency, functional stability and fatigue issue.^{2,12,22} The martensitic transformation is always accompanied by large thermal and stress hysteresis. Arising from the intrinsic energy dissipation, the hysteresis would significantly decrease the cooling efficiency and damage the fatigue property.^{17,23-24} In addition, elastocaloric effect of SMAs normally degrades with cyclic mechanical loadings. In Ni-Ti films, the stress induced adiabatic temperature change (ΔT) considerably decreases by 40% during the first 30 cycles.²⁵ This functional degradation is ascribed to the formation of dislocations during the martensitic transformation, which reduces the fraction of transformed martensite and leads to the decreased ΔT . For boosting the application of elastocaloric refrigeration, the design of practical cooling device also imposes a high demand on the mechanical stability for SMAs.

Although Ni-Ti alloys could achieve a mechanical stability through the aid of cyclic training, the large stress hysteresis limits its cooling efficiency and potential application.⁸ Furthermore, the large critical stress over 500 MPa for Ni-Ti significantly constrains the device dimension and the associated system cooling capacity. For example, considering an aspect ratio of 5, defined as the length ratio between axial and radial direction, a 5 kN linear driver could only load Ni-Ti alloy with a mass of 16 g, corresponding to less than 16 W cooling capacity under current specific cooling power of elastocaloric cooling technology.²⁶ As a result, in the published works, only the low-dimensional Ni-Ti wires,⁸ tubes,²⁷ and films²⁸ can be utilized in the refrigeration prototypes. Also, these shapes favor the high heat transfer to the environment and therefore an increase of cooling power. In comparison, Ni-Fe-Ga-Co alloys that possess a significant lower critical stress and hysteresis make it as a talented energy-efficient candidate to refrigeration devices, especially for the

air conditioners which require large cooling capacity and high energy efficiency.¹⁸ In this work, we investigate the stability of mechanical behavior and elastocaloric effect for a [001] oriented Ni_{50.0}Fe_{19.0}Ga_{27.1}Co_{3.9} single crystal during 12,000 mechanical cycles. Based on the experimental results, the numerical simulation is conducted to compare the crucial parameters, such as COP and cooling capacity of Ni-Ti alloy with those of our Heusler single crystal.

■ RESULTS AND DISCUSSION

Phase Transformation Behavior. Figure 1a shows the DSC curves for the Ni_{50.0}Fe_{19.0}Ga_{27.1}Co_{3.9} single crystal. The exothermal and endothermal peaks represent the martensitic and austenitic transformations, respectively. The start and finish temperatures for the martensitic (M_s and M_f) and austenitic (A_s and A_f) transformation have been marked in the curves. The thermal hysteresis (defined as $\Delta T_{\text{hys}} = (A_s + A_f - M_s - M_f)/2$) for the phase transformations is determined to be 10 °C. The phase transformation behavior is also detected in zero-field-cooling (ZFC) and field-cooling (FCC) magnetization curves, as shown in Figure 1b. The reversible martensitic transformation is indicated by the sudden changes of magnetization with a thermal hysteresis. Due to different sample sizes and heating and cooling rates,²⁹⁻³⁰ the characteristic transformation temperatures and thermal hysteresis exhibited in the thermomagnetic curve are slightly lower than those in Figure 1a. Besides, the Curie transition of austenite is observed at $T_C = 89.3$ °C.

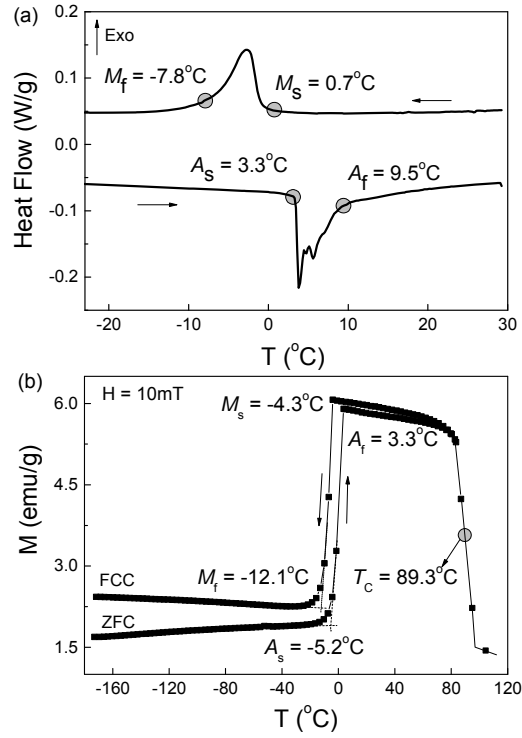


Figure 1. DSC curves (a) and thermomagnetic curve under the magnetic field of 10 mT (b) for the $\text{Ni}_{50.0}\text{Fe}_{19.0}\text{Ga}_{27.1}\text{Co}_{3.9}$ single crystal. The arrows indicate the direction of temperature change.

Superelastic Behavior and Fatigue Property. The fatigue property and mechanical stability of the $\text{Ni}_{50.0}\text{Fe}_{19.0}\text{Ga}_{27.1}\text{Co}_{3.9}$ single crystal at room temperature were investigated. According to previous studies,^{17-18,31-32} Ni-Fe-Ga-based alloys usually undergo a two-stage martensitic transformation as cubic austenite (with $L2_1$ atomic order) \rightarrow 10M/14M martensite (with 5/7 modulation period) \rightarrow tetragonal martensite (with $L1_0$ non-modulation lattice). Figure 2a presents the schematic structures of $L2_1$ austenite, $L1_0$ martensite, 10M martensite, and 14M martensite. Upon loading a uniaxial stress of 110 MPa, the two-stage transformation indicated by two successive stress plateaus is observed in our $\text{Ni}_{50.0}\text{Fe}_{19.0}\text{Ga}_{27.1}\text{Co}_{3.9}$ single crystal (indicated by the full loop), as shown in Figure 2b. The inter-martensitic transformation is accompanying with a large stress hysteresis, and thus is expected to drastically reduce the cooling efficiency.³³ In order to prevent the experience of inter-martensitic transformation, here we only loaded the target strain to a relatively

small value of 3.8% (small loop). In comparison of the stress-strain curves before and after cycling in Figure 2b, the $\text{Ni}_{50.0}\text{Fe}_{19.0}\text{Ga}_{27.1}\text{Co}_{3.9}$ single crystal shows an excellent mechanical stability at a strain rate of $0.02\% \text{ s}^{-1}$ and display fatigue-free superelastic behavior. Subjecting to over 12,000 cyclic tests, the stress-strain curve follows nearly the same path as the first cycle with a stable critical stress of 60 MPa and a small stress hysteresis of 9 MPa.

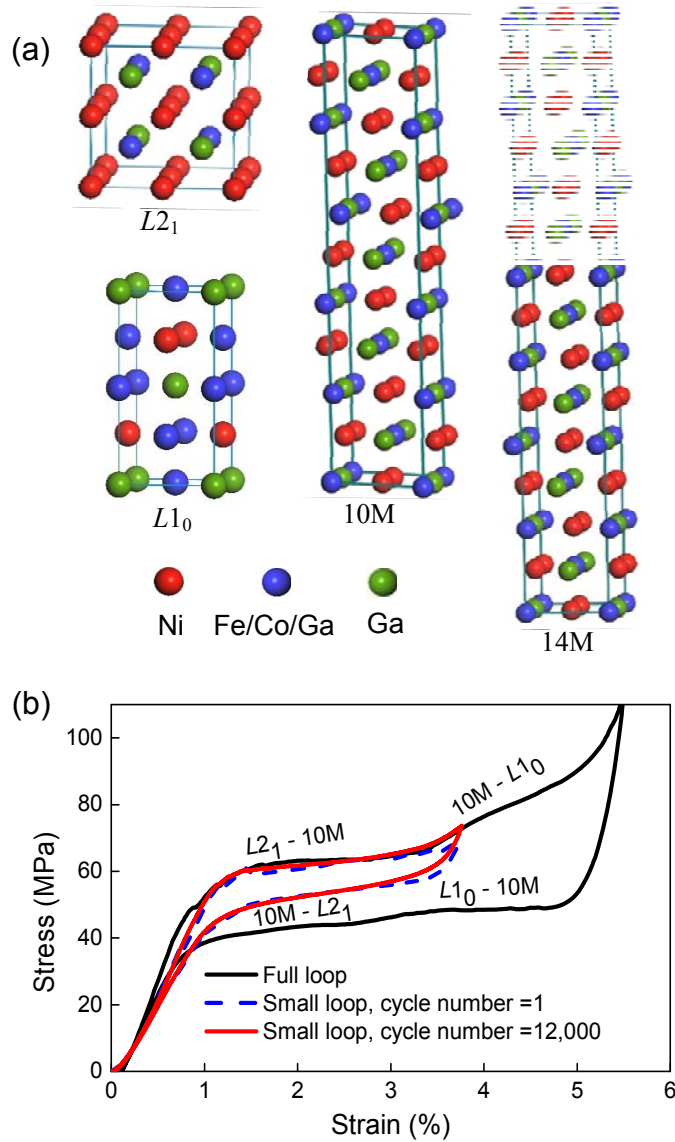


Figure 2. (a) Schematic structures of $L2_1$ austenite, $L1_0$ martensite, 10M martensite, and 14M martensite for the $\text{Ni}_{50.0}\text{Fe}_{19.0}\text{Ga}_{27.1}\text{Co}_{3.9}$ single crystal. (b) Isothermal stress-strain curves of the $\text{Ni}_{50.0}\text{Fe}_{19.0}\text{Ga}_{27.1}\text{Co}_{3.9}$ single crystal at room temperature with a strain rate of $0.02\% \text{ s}^{-1}$. Full loop for $L2_1$ -10M- $L1_0$ martensitic transformation and one-step $L2_1$ -10M martensitic transformation upon mechanical cycles are compared. The cycle numbers are indicated.

The crystallographic structure during the compressive test was studied by means of in situ neutron measurement. Figure 3a and b show the experimental setup of in-situ neutron diffraction and its corresponding schematic, respectively. The incoming beam size for the measurement is $5 \text{ mm} \times 5 \text{ mm}$. The application of uniaxial stress is realized through the rotatable load frame installed at STRESS-SPEC. Upon loading and unloading, the neutron diffraction data was recorded with an interval of

30 s by a two-dimensional detector at $2\theta = 61^\circ$. The resulting diffraction patterns are shown in Figure 3c. By increasing the stress from 0.5 to 53.3 MPa during the loading process, the diffraction peak of austenite $(220)_A$ at $2\theta = 61.3^\circ$ gradually broadens, which is very likely due to the increased internal stress in parent phase. The diffraction peak for martensitic phase $(125)_{10M}$ at 63.4° occurs at 53.3 MPa. The martensite induced by uniaxial stress is identified as a modulated type with five-layered structure (10M). Until the loading stress increases to 75.8 MPa, only the diffraction peak of martensite is observed, implying that the austenite has fully transformed into the martensite. Upon unloading, the martensitic peak vanishes at 40.9 MPa, indicating that the martensite entirely reverts back to the austenite. Thus, the excellent mechanical stability in the $\text{Ni}_{50.0}\text{Fe}_{19.0}\text{Ga}_{27.1}\text{Co}_{3.9}$ single crystal is caused by the reversible transformation from $L2_1$ austenite to 10M martensite.

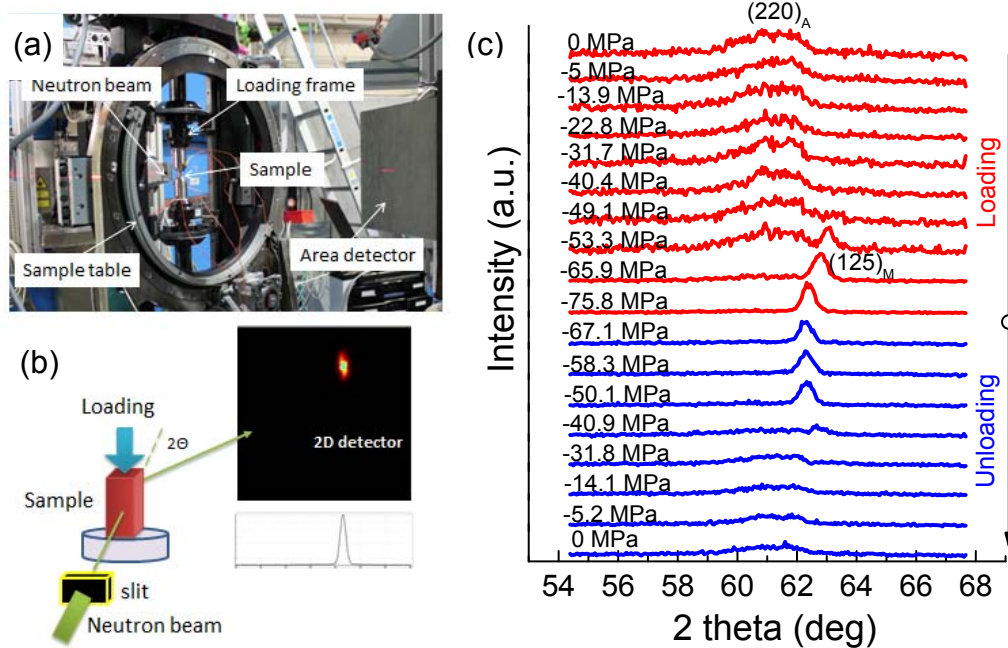


Figure 3. The unique compression rig installed at STRESS-SPEC for in situ neutron diffraction measurements (a) and its corresponding schematic (b), as well as the resulting diffraction patterns (c) for the $\text{Ni}_{50.0}\text{Fe}_{19.0}\text{Ga}_{27.1}\text{Co}_{3.9}$ single crystal during loading and unloading processes.

Elastocaloric Effect and Cycling Stability. Apart from the mechanical stability, the stability of elastocaloric effect (functional stability) for the $\text{Ni}_{50.0}\text{Fe}_{19.0}\text{Ga}_{27.1}\text{Co}_{3.9}$

single crystal was investigated. The cyclic compressive test (up to 12,000 cycles) was performed at a frequency of 1 Hz under a target stress of 130 MPa. The superelastic loops and temperature-time profiles recorded by infrared camera at different cycles are compared. The stress-strain curves during the high frequency compressive test in Figure 4a exhibit no significant degradation even after 12,000 cycles, suggesting a great mechanical stability. The increased stress hysteresis and transformation finishing stress should be due to the self-heating/self-cooling effect under adiabatic conditions. In such case, we assume that only the $L2_1$ austenite to 10M martensite phase transformation is utilized. Meanwhile, Figure 4b shows the maximum ΔT measured in the central region of the sample surface (marked as the rectangle area in Figure 4c). It reveals that ΔT keeps a constant level of 11 K without any degradation on the operation cycles. This indicates that our $\text{Ni}_{50.0}\text{Fe}_{19.0}\text{Ga}_{27.1}\text{Co}_{3.9}$ single crystal transforms highly repeatably through first-order transition. One should notice that the present temperature change measurement is not performed in a normal way, where after each loading and unloading step there should be sufficient time for the sample to stabilize with the surroundings. However, this is still a good way to demonstrate that our sample is able to generate relatively large temperature changes. Figure 4c shows a series of infrared images monitored from the entire surface of the sample during a single cycle. Upon loading, the formation of oriented martensite results in several parallel temperature bands at a 45° angle with respect to the loading direction. The transformed martensitic laths broaden in width with the increase of stress, correspondingly the temperature bands grow in size as well. Due to the propagation of phase boundaries and heat transfer spreading over the sample, the temperature homogenizes and ΔT reaches a maximum value of 11 K. Upon unloading, one austenitic region first occurs in the central warmer area and the temperature rapidly decreases. The temperature drop of about -11 K during unloading almost counteracts the temperature rising of +11 K on the loading stage.

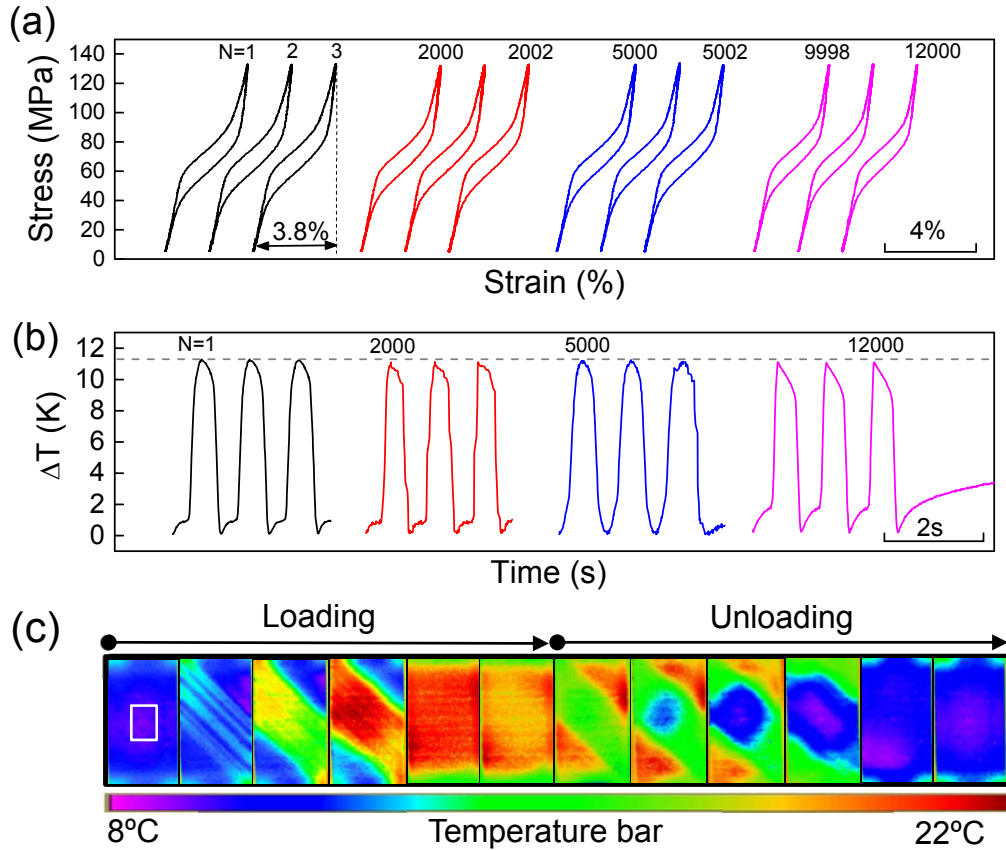


Figure 4. (a) The cyclic stress-strain curves of the $\text{Ni}_{50.0}\text{Fe}_{19.0}\text{Ga}_{27.1}\text{Co}_{3.9}$ single crystal at a high deformation frequency of 1 Hz under a target stress of 130 MPa. The cycle numbers are indicated. (b) Corresponding maximum ΔT measured by infrared camera in the central region of the sample at different cycles. (c) Series of infrared images of the sample surface during a typical cycle. The time interval between two adjacent images is about 0.1 s. The central region of the sample is marked as the white rectangle area in (c).

Structural Analysis. In our previous study, the elastocaloric effect of $\text{Ni}_{50}\text{Fe}_{19}\text{Ga}_{27}\text{Co}_4$ single crystal apparently decreases from 10 K to 7.2 K after 3,000 cycles.¹⁸ Also, Krooß et al. reported that the superelastic behavior of Co-Ni-Ga single crystal undergoes a dramatic degradation during 1,000 cyclic deformation.³⁴ In comparison, the present $\text{Ni}_{50.0}\text{Fe}_{19.0}\text{Ga}_{27.1}\text{Co}_{3.9}$ single crystal exhibits outstanding mechanical and functional stability. In order to obtain a deeper insight into the excellent stability, after fatigue test we further analyzed the martensitic structure by in situ transmission electron microscope. Figure 5 shows the bright-field images for the

$\text{Ni}_{50.0}\text{Fe}_{19.0}\text{Ga}_{27.1}\text{Co}_{3.9}$ single crystal cooling from 5 °C to -50 °C. The sample is in the austenitic state at 5 °C, and the martensitic plates start to grow at 0 °C. At -50 °C, there are fully martensite twins. Corresponding selected area electron diffraction (SAED) confirms an $L2_1$ superlattice structure for austenite. Apart from the main diffraction spots, the additional spots appear as the diffused pairwise reflection, positioning along the $\langle 110 \rangle$ direction, which is related to premartensitic transformation and phonon anomalies in the $[\zeta\zeta 0]$ TA_2 phonon branch.³⁵ The martensite can be indexed to be the modulated seven-layered structure (14M) with six satellite spots between the main diffraction spots. The striking feature indicates the presence of a structural transformation from a cubic to a monoclinic phase. It should be noticed that the deformation formed martensite with 10M structure revealed by the neutron measurement is different from thermally induced 14M martensite. It is well known that the dislocation motion governs functional degradation and superelastic stability of SMAs. Compared with Co-Ni-Ga³⁴ and $\text{Ni}_{50}\text{Fe}_{19}\text{Ga}_{27}\text{Co}_4$ ¹⁸ single crystals which represent non-modulated $L1_0$ martensite, in this work, the modulated martensitic structure with a high density of micro-twins normally owns the low twin boundary energy, and also a relative small lattice misfit between austenite and martensite, thus it is prone to reduce the critical transformation stress and prolong the fatigue life. Therefore, the $\text{Ni}_{50.0}\text{Fe}_{19.0}\text{Ga}_{27.1}\text{Co}_{3.9}$ single crystal has superior mechanical and functional stabilities.

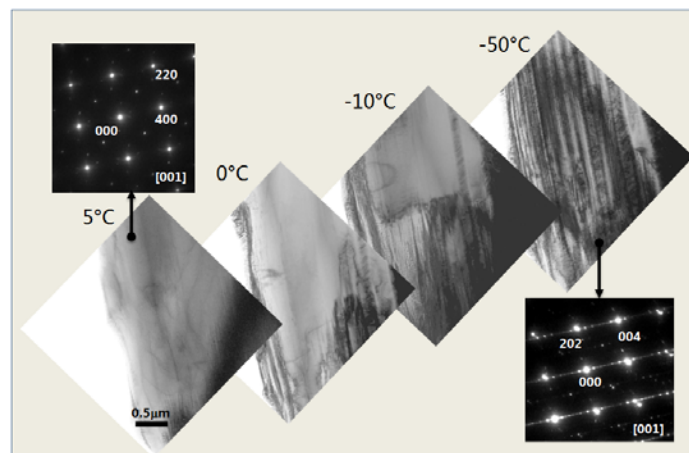


Figure 5. TEM bright field images of the $\text{Ni}_{50.0}\text{Fe}_{19.0}\text{Ga}_{27.1}\text{Co}_{3.9}$ single crystal taken at different temperatures and the corresponding selected area electron diffraction for the austenitic structure at 5 °C and martensitic structure at -50 °C.

We additionally checked the compatibility conditions of the microstructure formed during the phase transformation, which are determined by the structural parameters of the austenitic and martensitic phases.³⁶⁻³⁸ The precise measurement of symmetries and the corresponding lattice parameters was conducted by the synchrotron X-ray Laue micro-diffraction. Figure 6 shows the diffraction patterns of austenite and martensite indexed by the cubic and monoclinic structure respectively. We used these Laue patterns as the references for the monochromatic energy scan that determines the lattice parameters as $a_0 = 0.5759$ nm for the cubic austenite, and $a = 0.4326$ nm, $b = 0.5435$ nm, $c = 0.4189$ nm, $\beta = 85.987^\circ$ for the monoclinic martensite. Using the StrucTrans algorithm,³⁶ we determined the set of compatibility conditions: i) the middle eigenvalue of the transformation stretch tensor λ_2 as 1.00334, and ii) for (101) type I twin, the cofactor condition (CCI) is calculated as 0.000539359. These values approach the ideal case ($\lambda_2 = 1$ and $\text{CCI}=0$), implying that our single crystal can undergo a compatible transformation by surviving a large number of reversible cycles without deleterious effect.³⁷⁻³⁸

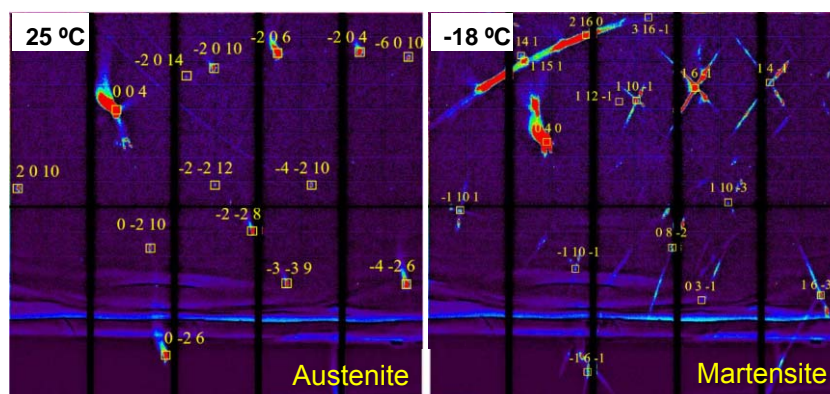


Figure 6. Laue patterns of austenite at 25 °C and martensite at -18 °C.

Cooling performance. For the energy-efficient refrigeration application, a good elastocaloric material must exhibit superior system performance in addition to its remarkable mechanical and functional stability. When comparing to the

state-of-the-art nitinol alloy, from system operating point of view, the novel $\text{Ni}_{50.0}\text{Fe}_{19.0}\text{Ga}_{27.1}\text{Co}_{3.9}$ single crystal alloy demonstrates larger COP, as well as more cooling capacity under the constraint of identical driving force. The high efficient system COP is a direct result of the small hysteresis during the stress-induced martensitic transformation in the Ni-Fe-Ga-Co alloy, representing less phase change irreversibility than the conventional nitinol alloy. In this study, a previously developed numerical model for a single-stage elastocaloric cooling system is used to evaluate the performance enhancement potential of Ni-Fe-Ga-Co.^{27,39} The predicted temperature variations of the numerical model were validated by experimental data from a prototype with small deviations.⁴⁰ The dynamic system model considered the coupled phase transformation and heat transfer of the elastocaloric material, the fluid flowing inside and the associated heat transfer fluid network. Cooling capacity and COP can be evaluated based on the predicted temperature evolution profiles from the model. A system with tube-shape elastocaloric materials is evaluated for both nitinol and Ni-Fe-Ga-Co, under the 5 K system temperature lift and 0.2 m/s fluid flow velocity conditions. We should emphasize that Ni-Fe-Ga-based alloys show considerable formability by hot deformation,⁴¹ thus they hold a great potential for fabricating into tubes with desirable dimensions used for modelling. As illustrated in Figure 7a, the system with Ni-Fe-Ga-Co alloy shows the maximum of 18% efficiency improvement. It also implies that the system with $\text{Ni}_{50.0}\text{Fe}_{19.0}\text{Ga}_{27.1}\text{Co}_{3.9}$ prefers low cycling frequency condition. This phenomenon is a comprehensive interaction of materials latent heat, materials hysteresis, and heat transfer performance. Since the adiabatic temperature change and latent heat of Ni-Fe-Ga-Co are unfortunately less than those of the nitinol alloy, it requires longer time to release the same amount of cooling capacity for system with Ni-Fe-Ga-Co alloy under identical heat transfer conditions. Furthermore, in real elastocaloric cooling systems, the overall dimensions are usually determined by their drivers, which are directly related to the loading force required by the phase transformation stress of the elastocaloric materials in systems.

$\text{Ni}_{50.0}\text{Fe}_{19.0}\text{Ga}_{27.1}\text{Co}_{3.9}$ with its maximum of 140 MPa loading stress is capable to be loaded by an identical driver with 400% more material mass than the nitinol alloy. Consequently, given the same driver, a system equipped with Ni-Fe-Ga-Co alloy is expected to perform 70% more cooling capacity than that with nitinol alloy, as shown in Figure 7b. The performance curve of Ni-Fe-Ga-Co alloy has a maximum value at cycle duration of 12 seconds, as a result of the following two competing factors. The cooling capacity increases with less cycle duration since more cycles can be operated within a specific time frame. However, the heat transfer in each cycle becomes less efficient when cycling frequency increases. Consequently, heat transfer efficiency is the dominating factor when cycling duration is less than 12 seconds. Furthermore, with identical material geometries, Ni-Fe-Ga-Co only requires 20% of the driver's loading force when compared to nitinol. In fact, this unique advantage of Ni-Fe-Ga-Co alloy can be expected to attract much attention since it is quite convenient to apply in realistic demonstration prototypes. For example, a regular linear motor with 5 kN loading capacity is capable to drive sufficient amount of Ni-Fe-Ga-Co alloy to provide close to 30 W cooling capacity. In addition, the aforementioned simulation was conducted assuming both materials are in tube shape with 0.5 mm wall thickness and water as heat transfer fluid flowing inside, wherein the porosity is close to 0.64.²⁷ Elastocaloric materials with other shapes, thinner walls and the active regeneration scheme²⁶ could lead to even higher cycling frequency and performance than the demonstrated conditions in Figure 4, which should be further investigated in details by future studies.

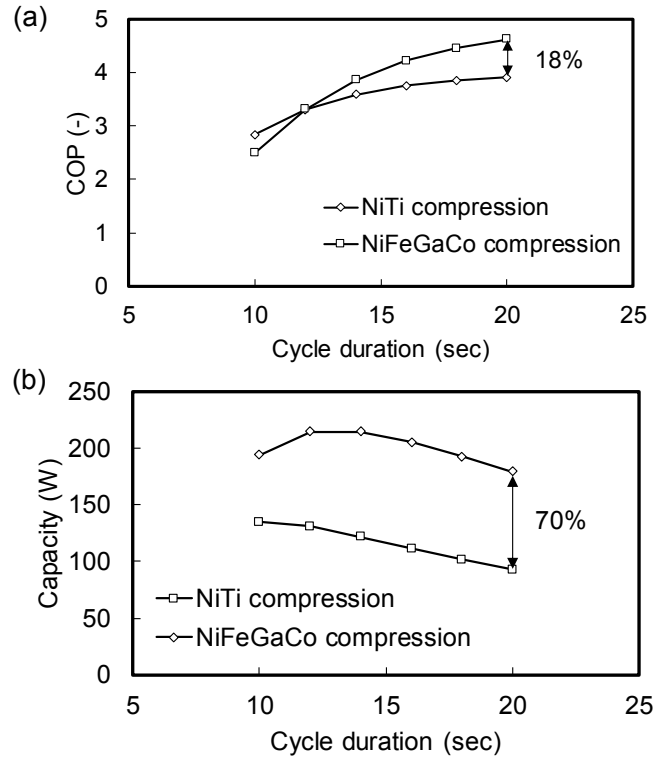


Figure 7. Model predicted COP (a) and cooling capacity (b) for Ni-Ti and $\text{Ni}_{50.0}\text{Fe}_{19.0}\text{Ga}_{27.1}\text{Co}_{3.9}$ single crystal as a function of cycle duration.

■ CONCLUSIONS

In summary, the mechanical and functional stability of the $\text{Ni}_{50.0}\text{Fe}_{19.0}\text{Ga}_{27.1}\text{Co}_{3.9}$ single crystal have been investigated. Due to the flexibly and reversibly transferring interface, the $\text{Ni}_{50.0}\text{Fe}_{19.0}\text{Ga}_{27.1}\text{Co}_{3.9}$ single crystal shows ultralow fatigue, superior stability of superelastic behavior and elastocaloric effect. A local ΔT keeps a maximum value of 11 K during above 12,000 cycles. Further investigation on more cycles should be designed in order to precisely compare the fatigue properties with Ni-Ti alloys.⁴² The phase transformation and crystallographic structures are studied by in situ neutron diffraction measurement, in situ TEM and in situ synchrotron X-ray micro-diffraction. Furthermore, we utilize a previously developed numerical model to evaluate and compare the cooling performance of Ni-Fe-Ga-Co alloy with that of Ni-Ti alloy. The numerical simulation results indicate that the $\text{Ni}_{50.0}\text{Fe}_{19.0}\text{Ga}_{27.1}\text{Co}_{3.9}$ single crystal developed in this study offers 18% energy saving potential and 70%

cooling capacity enhancement potential than the conventional nitinol alloy in a single-stage elastocaloric cooling system, making it as a promising candidate for the energy-efficient refrigerator and air conditioner.

■ EXPERIMENT

Ingots of $\text{Ni}_{50.0}\text{Fe}_{19.0}\text{Ga}_{27.1}\text{Co}_{3.9}$ (at.%) alloy were prepared by arc melting in argon atmosphere from high pure Ni (99.99%), Fe (99.99%), Ga (99.99%) and Co (99.99%). Single crystal was grown by Bridgman technique in an inert atmosphere. Rectangular samples in size of $3.9 \text{ mm} \times 3.9 \text{ mm} \times 7.9 \text{ mm}$ with the long axis along the $[001]_A$ -direction (A represents the parent austenite phase) for compressive tests were cut by electro-discharge machining from the single crystal. Phase transformation of the single crystal was characterized by a superconducting quantum interference device (SQUID, Quantum Design MPMS-5S) and a Pyris Diamond differential scanning calorimeter (DSC, Perkin-Elmer). The heating/cooling rate for the DSC measurement is 10 K/min. Thermal conductivity was measured at room temperature using a laser-flash thermal conductivity apparatus (LFA). Microstructure of the sample under different operating temperatures was observed by transmission electron microscope (JOEL 2100 HR TEM) at different operating temperatures. The lattice parameters of the specimen were measured by the synchrotron X-ray diffraction at the Beamline 12.3.2, Advanced Light Source, Lawrence Berkeley Nation Lab. The detail of the experimental process has been described elsewhere.⁴³ The disk was spark cut from the sample subjected to the cyclic compressive test. The crystal structure of the $\text{Ni}_{50.0}\text{Fe}_{19.0}\text{Ga}_{27.1}\text{Co}_{3.9}$ alloy under compressive test was determined using an in situ neutron measurement. The materials science diffractometer STRESS-SPEC was operated by FRM II and HZG at the Heinz Maier-Leibnitz Zentrum, Garching, Germany, with a monochromatic wavelength of 2.1 \AA .⁴⁴ The cyclic compressive experiments were performed with force-controlled mode at a frequency of 1 Hz on a testing machine (Autograph AG-I 50 kN MODEL M1, Shimadzu). The stress-induced ΔT of the sample was monitored by a high-resolution infrared camera with a frame

rate of 115 Hz. Sample was covered with a thin layer of black spray on the surface to improve thermal emissivity. Besides, before and after the cyclic compressive experiments, isothermal compression experiments were conducted with strain-controlled mode on a universal testing machine (SUN UTM5000). The isothermal stress-strain curves were recorded with a strain rate of 0.02% s⁻¹ at 17 °C.

■ NUMERICAL MODEL

The numerical model used in this study was based on the one-dimensional energy equations derived from the dynamic phase transformation and heat exchange processes of the elastocaloric material bed, as shown in the following equations.²⁷ The energy equations are similar to those used in literature for elastocaloric cooling systems,⁴⁵ except for minor difference of the phase transformation model. Furthermore, the fluid network configuration and control strategy for the system operation in this study were set to follow the single-stage Brayton cycle, which were different from the active regenerator cycle as discussed by Tusek et al.⁴⁵ There is a tradeoff between the two cycles. A single-stage Brayton cycle with heat recovery theoretically has better COP, but suffers the small system temperature lift, when compared to the active regenerator cycle.

$$(1-\varepsilon)\frac{\partial T_s}{\partial t} = (1-\varepsilon)\alpha_s \frac{\partial^2 T_s}{\partial x^2} - \frac{h\beta}{(\rho c_p)_s}(T_s - T_f) + (1-\varepsilon)\frac{g'''}{(\rho c_p)_s} \quad (1)$$

$$\varepsilon \frac{\partial T_f}{\partial t} = \varepsilon\alpha_f \frac{\partial^2 T_f}{\partial x^2} - \frac{4h\beta}{(\rho c_p)_f}(T_f - T_s) - \varepsilon u_f \frac{\partial T_f}{\partial x} \quad (2)$$

wherein T_s , T_f are local average temperature of the SMA and heat exchange fluid, respectively. The g''' term stands for the dynamic elastocaloric effect, which is determined by the phase change model. The ρ is the density of SMA. The thermal conductivity k_s and specific heat c_p were measured by LFA. In this study, a simple homogenous phase change model for a single-crystal was applied. The heat transfer coefficient h is determined based on Nusselt number of 3.66 for laminar internal flow. The specific heat transfer area β is set to be 640 m²/m³, which is defined as the ratio

between specific heat transfer area and volume of entire bed. The porosity ε is set to be 0.64. Properties of water at temperature of 20°C are used for the heat transfer fluid. The phenomenological superelastic model with Maxwell relation and Clausius-Clapeyron equation to predict the elastocaloric effect term is another viable option, which may over-predict the elastocaloric effect since the eCE is not directly measured.⁴⁵ More details regarding the thermal properties can be found in Table 1. Besides, the following assumptions are made deriving the numerical model used in this study.

- The timescales of phase transformation and loading are negligible compared with that of heat transfer.
- Conductive heat transfer in radial direction is negligible compared with that in axial direction.
- Uniaxial loading and uniform phase transformation.
- Constant thermophysical properties within the small temperature range of interest.
- Incompressible flow and uniform velocity profile at any cross section inside the SMA tube.
- Uniform fluid temperature profile at any cross section inside the SMA tube.
- No heat transfer from SMA tubes to surrounding.
- No radiation heat transfer.

The partial differential equations were discretized with 50 spatial nodes for the elastocaloric material, wherein the central difference scheme and second-order upwind scheme were applied for the diffusion terms and convective terms, respectively. The derived discretized equations were modeled in MATLAB Simulink® environment. The time variable was solved by fixed-time step Ronge-Kutta solver with the Forward Euler Method. Time step of 0.001 s was applied to the solver. The numerical model predictions were extensively validated by experimental data in a water-cooled elastocaloric cooling prototype.⁴⁶ For this reason,

the same geometric parameters were used in this study, i.e. elastocaloric material tubes with outer diameter of 5mm and inner diameter of 4mm. In each performed simulation study, the initial condition for all of the nodes in the model is set to 20°C. All simulations were evaluated for at least 100 cycles to ensure the cyclic steady state condition before performance indices were sampled. A system temperature lift of 5 K was set to compare the system performance of nitinol and the novel Ni-Fe-Ga-Co alloy, which implied that the heat sink was set to 22.5°C and the heat source was set to 17.5°C.

Table 1. Properties used in the numerical model.

	Ni-Fe-Ga-Co	Ni-Ti
Thermal conductivity k_s [W/m·K]	17.38	18.0
Specific heat c_p [J/g·K]	0.45	0.50
Density ρ [g/cm ³]	8.86	6.50
Δs [J/g·K]	0.018	0.042
Loading work (compression) [J/g]	1.572	4.05 ¹²
Unloading work (compression) [J/g]	1.233	2.82 ¹²

■ AUTHOR INFORMATION

Corresponding Author

*E-mail: liujian@nimte.ac.cn; qiansuxin@xjtu.edu.cn

ORCID

Jian Liu: 0000-0001-5658-5958

Author Contributions

[†]Yang Li and Dewei Zhao contribute equally to this work.

Notes

The authors declare no competing financial interest.

■ ACKNOWLEDGMENTS

The research leading to these results has received funding from the National Key Research and Development Program of China (Grant No. 2017YFB0702703), the External Cooperation Program of Chinese Academy of Sciences (Grant No. 174433KYSB20180040), and the National Natural Science Foundation of China (Grant Nos. 51771218, 51531008 and 51606140). Authors thank the fruitful discussion with A. Planes and L. Mañosa from University of Barcelona.

■ REFERENCES

- (1) Kitanovski, A.; Plaznik, U.; Tomc, U.; Poredoš, A. Present and Future Caloric Refrigeration and Heat Pump Technologies. *Int. J. Refrig.* **2015**, *57*, 288-298.
- (2) Fähler, S.; Rößler, U. K.; Kastner, O.; Eckert, J.; Eggeler, G.; Emmerich, H.; Entel, P.; Müller, S.; Quandt, E.; Albe, K. Caloric Effects in Ferroic Materials: New Concepts for Cooling. *Adv. Eng. Mater.* **2012**, *14*, 10-19.
- (3) Mañosa, L.; Planes, A.; Acet, M. Advanced Materials for Solid-state Refrigeration. *J. Mater. Chem. A* **2013**, *1*, 4925-4936.
- (4) Moya, X.; Kar-Narayan, S.; Mathur, N. D. Caloric Materials Near Ferroic Phase Transitions. *Nat. Mater.* **2014**, *13*, 439-450.
- (5) Mischenko, A. S.; Zhang, Q.; Scott, J. F.; Whatmore, R. W.; Mathur, N. D. Giant Electrocaloric Effect in Thin Film $\text{PbZr}_{0.95}\text{Ti}_{0.05}\text{O}_3$. *Science* **2006**, *311*, 1270-1271.
- (6) Neese, B.; Chu, B.; Lu, S.-G.; Wang, Y.; Furman, E.; Zhang, Q. M. Large Electrocaloric Effect in Ferroelectric Polymers Near Room Temperature. *Science* **2008**, *321*, 821-823.
- (7) Pecharsky, V. K.; Gschneidner, K. A. $\text{Gd}_5(\text{Si}_x\text{Ge}_{1-x})_4$: An Extremum Material. *Adv. Mater.* **2001**, *13*, 683-686.
- (8) Tušek, J.; Engelbrecht, K.; Mikkelsen, L. P.; Pryds, N. Elastocaloric Effect of Ni-Ti Wire for Application in a Cooling Device. *J. Appl. Phys.* **2015**, *117*, 124901.
- (9) Zimm, C.; Jastrab, A.; Sternberg, A.; Pecharsky, V.; Gschneidner, K.; Osborne, M.; Anderson, I. Description and Performance of a Near-room Temperature Magnetic Refrigerator. *Adv. Cryog. Eng.* **1998**, *43*, 1759-1766.
- (10) Gu, H. M.; Qian, X. S.; Li, X. Y.; Craven, B.; Zhu, W. Y.; Cheng, A. L.; Yao, S. C.; Zhang, Q. M. A Chip Scale Electrocaloric Effect Based Cooling Device. *Appl. Phys. Lett.* **2013**, *102*, 122904.
- (11) Gschneidner, K. A.; Pecharsky, V. K. Thirty Years of Near Room Temperature

- Magnetic Cooling: Where We Are Today and Future Prospects. *Int. J. Refrig.* **2008**, 31, 945-961.
- (12) Cui, J.; Wu, Y.; Muehlbauer, J.; Hwang, Y.; Radermacher, R.; Fackler, S.; Wuttig, M.; Takeuchi, I. Demonstration of High Efficiency Elastocaloric Cooling with Large ΔT Using NiTi Wires. *Appl. Phys. Lett.* **2012**, 101, 073904.
- (13) Goetzler, W.; Zogg, R.; Young, J.; Johnson, C. Energy Savings Potential and RDD Opportunities for Non-Vapor-Compression HVAC Technologies, prepared for U.S. Department of Energy. Navigant Consulting Inc. **2014**.
- (14) Ossmer, H.; Lambrecht, F.; Gültig, M.; Chluba, C.; Quandt, E.; Kohl, M. Evolution of Temperature Profiles in TiNi Films for Elastocaloric Cooling. *Acta Mater.* **2014**, 81, 9-20.
- (15) Mañosa, L.; Jarque-Farnos, S.; Vives, E.; Planes, A. Large Temperature Span and Giant Refrigerant Capacity in Elastocaloric Cu-Zn-Al Shape Memory Alloys. *Appl. Phys. Lett.* **2013**, 103, 211904.
- (16) Xu, Y.; Lu, B. F.; Sun, W.; Yan, A.; Liu, J. Large and Reversible Elastocaloric Effect in Dual-phase Ni₅₄Fe₁₉Ga₂₇ Superelastic Alloys. *Appl. Phys. Lett.* **2015**, 106, 201903.
- (17) Li, Y.; Zhao, D. W.; Liu, J. Giant and Reversible Room-temperature Elastocaloric Effect in a Single-crystalline Ni-Fe-Ga Magnetic Shape Memory Alloy. *Sci. Rep.* **2016**, 6, 25500.
- (18) Xiao, F.; Jin, M. J.; Liu, J.; Jin, X. J. Elastocaloric Effect in Ni₅₀Fe₁₉Ga₂₇Co₄ Single Crystals. *Acta Mater.* **2015**, 96, 292-300.
- (19) Xiao, F.; Fukuda, T.; Kakeshita, T. Significant Elastocaloric Effect in a Fe-31.2Pd (at.%) Single Crystal. *Appl. Phys. Lett.* **2013**, 102, 161914.
- (20) Lu, B. F.; Xiao, F.; Yan, A. R.; Liu, J. Elastocaloric Effect in a Textured Polycrystalline Ni-Mn-In-Co Metamagnetic Shape Memory Alloy. *Appl. Phys. Lett.* **2014**, 105, 161905.
- (21) Sun, W.; Liu, J. Lu, B. F.; Yan, A. R. Large Elastocaloric Effect at Small

- Transformation Strain in $\text{Ni}_{45}\text{Mn}_{44}\text{Sn}_{11}$ Metamagnetic Shape Memory Alloys. *Scr. Mater.* **2016**, 114, 1-4.
- (22) Chluba, C.; Ge, W. W.; Miranda, R. L. de; Strobel, J.; Kienle, L.; Quandt, E.; Wuttig, M. Ultralow-fatigue Shape Memory Alloy Films. *Science* **2015**, 348, 1004-1007.
- (23) Hamilton, R. F.; Sehitoglu, H.; Efstathiou, C.; Maier, H. J.; Chumlyakov, Y. Pseudoelasticity in Co-Ni-Al Single and Polycrystals. *Acta Mater.* **2006**, 54, 587-599.
- (24) Hamilton, R. F.; Sehitoglu, H.; Chumlyakov, Y.; Maier, H. J. Stress Dependence of the Hysteresis in Single Crystal NiTi Alloys. *Acta Mater.* **2004**, 52, 3383-3402.
- (25) Bechtold, C.; Chluba, C.; Miranda, R. L. de; Quandt, E. High Cyclic Stability of the Elastocaloric Effect in Sputtered TiNiCu Shape Memory Films. *Appl. Phys. Lett.* **2012**, 101, 091903.
- (26) Tušek, J.; Engelbrecht, K.; Eriksen, D.; Dall'Olio, S.; Tušek, J.; Pryds, N. A Regenerative Elastocaloric Heat Pump. *Nat. Energy* **2016**, 101, 16134.
- (27) Qian, S. X.; Ling, J. Z.; Hwang, Y. H.; Radermacher, R.; Takeuchi, I. Thermodynamics Cycle Analysis and Numerical Modeling of Thermoelastic Cooling Systems. *Int. J. Refrig.* **2015**, 56, 65-80.
- (28) Ossmer, H.; Wendler, F.; Gueltig, M.; Lambrecht, F.; Miyazaki, S.; Kohl, M. Energy-efficient Miniature-scale Heat Pumping Based on Shape Memory Alloys. *Smart Mater. Struct.* **2016**, 25, 085037.
- (29) Srivastava, V.; Chen, X.; James, R. D. Hysteresis and Unusual Magnetic Properties in the Singular Heusler Alloy $\text{Ni}_{45}\text{Co}_5\text{Mn}_{40}\text{Sn}_{10}$. *Appl. Phys. Lett.* **2010**, 97, 014101.
- (30) Nayak, A. K.; Suresh, K. G.; Nigam, A. K. Metastability of Magneto-structural Transition Revealed by Sweep Rate Dependence of Magnetization in $\text{Ni}_{45}\text{Co}_5\text{Mn}_{38}\text{Sb}_{12}$ Heusler Alloy. *J. Appl. Phys.* **2011**, 109, 07A906.
- (31) Sutou, Y.; Kamiya, N.; Omori, T.; Kainuma, R.; Ishida, K.; Oikawa, K.

- Stress-strain Characteristics in Ni-Ga-Fe Ferromagnetic Shape Memory Alloys. *Appl. Phys. Lett.* **2004**, 84, 1275.
- (32) Timofeeva, E. E.; Panchenko, E. Y.; Chumlyakov, Y. I.; Tagiltsev, A. I. Intermartensitic Thermoelastic Transformations in [012]-Oriented Single Crystals of Ferromagnetic NiFeGa Alloys Under Compressive Loading. *Russ. Phys. J.* **2015**, 57, 1268-1277.
- (33) Bruno, N. M.; Karaman, I.; Chumlyakov, Y. I. Orientation Dependence of the Elastocaloric Effect in Ni₅₄Fe₁₉Ga₂₇ Ferromagnetic Shape Memory Alloy. *Phys. Status Solidi B* **2017**, 255, 1700437.
- (34) Krooß, P.; Kadletz, P. M.; Somsen, C.; Gutmann, M. J.; Chumlyakov, Y. I.; Schmahl, W. W.; Maier, H. J.; Niendorf, T. Cyclic Degradation of Co₄₉Ni₂₁Ga₃₀ High-Temperature Shape Memory Alloy: On the Roles of Dislocation Activity and Chemical Order. *Shap. Mem. Superelasticity* **2016**, 2, 37-49.
- (35) Liu, L. B.; Fu, S. Y.; Liu, Z. H.; Wu, G. H.; Sun, X. D.; Li, J. Q. Microstructure and Low-temperature Phase Transition in Ni₂FeGa Heusler Alloy. *J. Alloys Compd.* **2006**, 425, 176-180.
- (36) Chen, X.; Song, Y.; Tamura, N.; James, R. D. Determination of the Stretch Tensor for Structural Transformations. *J. Mech. Phys. Solids* **2016**, 93, 34-43.
- (37) Chen, X.; Srivastava, V.; Dabade, V.; James, R. D. Study of the Cofactor Conditions: Conditions of Supercompatibility between Phases. *J. Mech. Phys. Solids* **2013**, 61, 2566-2587.
- (38) Song, Y.T.; Chen, X.; Dabade, V.; Shield, T. W.; James, R. D. Enhanced Reversibility and Unusual Microstructure of a Phase-transforming Material. *Nature* **2013**, 502, 85-88.
- (39) Qian, S. X.; Alabdulkarem, A.; Ling, J. Z.; Muehlbauer, J.; Hwang, Y.; Radermacher, R.; Takeuchi, I. Performance Enhancement of a Compressive Thermoelastic Cooling System Using Multi-objective Optimization and Novel Designs. *Int. J. Refrig.* **2015**, 57, 62-76.

- (40) Qian, S. X. Development of Thermoelastic Cooling Systems, University of Maryland (Doctoral thesis) **2015**.
- (41) Biswas, A.; Singh, G.; Sarkar, S. K.; Krishnan, M.; Ramanurty, U. Hot Deformation Behavior of Ni-Fe-Ga-based Ferromagnetic Shape Memory Alloy-A Study Using Processing Map. *Intermetallics* **2014**, 54, 69-78.
- (42) Tušek, J.; Žerovnik, A.; Čebren, M.; Brojan, M.; Žužek, B.; Engelbrecht, K.; Cadelli, A. Elastocaloric effect vs Fatigue Life: Exploring the Durability Limits of Ni-Ti Plates under Pre-strain Conditions for Elastocaloric Cooling. *Acta Mater.* **2018**, 150, 295-307.
- (43) Zhao, D. W.; Liu, J.; Chen, X.; Sun, W.; Li, Y.; Zhang, M. X.; Shao, Y. Y.; Zhang, H.; Yan, A. R. Giant Caloric Effect of Low-hysteresis Metamagnetic Shape Memory Alloys with Exceptional Cyclic Functionality. *Acta Mater.* **2017**, 133, 217-223.
- (44) Brokmeier, H. G.; Gan, W. M.; Randau, C.; Völler, M.; Rebelo-Kornmeier, J.; Hofmann, M. Texture Analysis at Neutron Diffractometer STRESS-SPEC. *Nucl. Instrum. Methods Phys. Res., Sect. A* **2011**, 642, 87-92.
- (45) Tušek, J.; Engelbrecht, K.; Millán-Solsona, R.; Mañosa, L.; Vives, E.; Mikkelsen, L. P.; Pryds, N. The Elastocaloric Effect: A Way to Cool Efficiently. *Adv. Energy Mater.* **2015**, 5, 1500361.
- (46) Qian, S. X.; Geng, Y. L.; Wang, Y.; Muehlbauer, J.; Ling, J.; Hwang, Y.; Radermacher, R.; Takeuchi, I. Design of a Hydraulically Driven Compressive Elastocaloric Cooling System. *Sci. Technol. Built En.* **2016**, 22, 500-506.